Premixed Flame Kernel Development under Engine Conditions based on DNS Data - Supplementary Material -

T. Falkenstein[1], S. Kang[2] and H. Pitsch[1]†

[1]Institute for Combustion Technology, RWTH Aachen University, 52056 Aachen, Germany
[2]Department of Mechanical Engineering, Sogang University, Seoul 121-742, Republic of Korea

(Received xx; revised xx; accepted xx)

1. Approximation of the Curvature Stretch Term

In the following, justification for omitting the correlations between κ and the normal displacement speed s_{rn}, as well as between κ^2 and the the thermal diffusivity D_{th} in (1.9) and (1.10) in the paper will be provided. Wang *et al.* (2017) investigated the correlation between curvature and displacment speed along the axial direction of a premixed jet flame using the following decomposition of the curvature stretch term:

$$\langle s_d \kappa \rangle_s = \langle s_d \rangle_s \langle \kappa \rangle_s + \left[\langle s_d \kappa \rangle_s - \langle s_d \rangle_s \langle \kappa \rangle_s \right]. \tag{S-1.1}$$

All terms in (S-1.1) have been evaluated in the planar-flame dataset discussed in the paper, as well as in an identical flame computed with non-unity Lewis numbers. Wang *et al.* (2017) have shown that the correlation between displacement speed and curvature, quantified by $[\langle s_d \kappa \rangle_s - \langle s_d \rangle_s \langle \kappa \rangle_s]$, dominates the r.h.s. of (S-1.1), which is confirmed by the results provided in figure S-1 (a).

The displacement speed s_d can be expressed by a normal-propagation velocity s_{rn} and a curvature term, after splitting the diffusion term of the reaction progress variable ζ into contributions by normal and tangential diffusion (Echekki & Chen 1999):

$$s_d = \frac{1}{\rho |\nabla \zeta|} \left(\dot{\omega}_\zeta - \frac{\partial}{\partial x_n} \left(\rho D_{th} |\nabla \zeta| \right) \right) - D_{th} \kappa = s_{rn} - D_{th} \kappa. \tag{S-1.2}$$

Hence, the curvature stretch term can be rewritten as

$$\langle s_d \kappa \rangle_s = \langle s_{rn} \kappa \rangle_s - \left\langle D_{th} \kappa^2 \right\rangle_s. \tag{S-1.3}$$

Now, each term in the r.h.s. of (S-1.3) may be separately decomposed in analogy to (S-1.1):

$$\langle s_{rn} \kappa \rangle_s = \langle s_{rn} \rangle_s \langle \kappa \rangle_s + \left[\langle s_{rn} \kappa \rangle_s - \langle s_{rn} \rangle_s \langle \kappa \rangle_s \right], \tag{S-1.4}$$

$$- \left\langle D_{th} \kappa^2 \right\rangle_s = - \langle D_{th} \rangle_s \left\langle \kappa^2 \right\rangle_s - \left[\left\langle D_{th} \kappa^2 \right\rangle_s - \langle D_{th} \rangle_s \left\langle \kappa^2 \right\rangle_s \right]. \tag{S-1.5}$$

In figure S-1 (b) it is shown that approximating $\langle s_{rn} \kappa \rangle_s$ by $\langle s_{rn} \rangle_s \langle \kappa \rangle_s$ is not very accurate during flame development in general and in the non-unity-Lewis-number flame in particular. When the unity-Lewis-number flame is fully developed, the correlation between the normal propagation velocity and curvature is rather weak. However, the contribution of the normal-propagation term $\langle s_{rn} \kappa \rangle_s$ to the overall curvature stretch effect is quite

† Email address for correspondence: office@itv.rwth-aachen.de

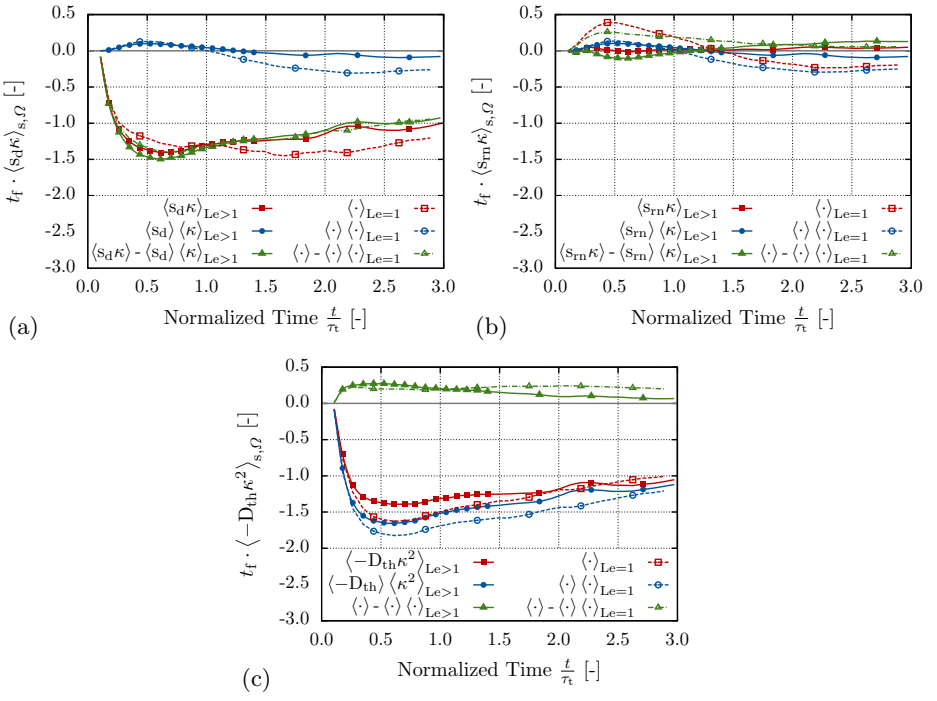

FIGURE S-1. Contributions to the curvature stretch term as function of time.

small due to the cancellation of terms from positively and negatively curved flame regions (Falkenstein *et al.* 2019). By contrast, the scalar dissipation term $-\langle D_{\mathrm{th}} \kappa^2 \rangle_{\mathrm{s}}$ is the dominant curvature stretch effect under the present conditions as shown in figure S-1 (c). Further, neglecting the correlation between the thermal diffusivity and curvature magnitude $\left[\langle D_{\mathrm{th}} \kappa^2 \rangle_{\mathrm{s}} - \langle D_{\mathrm{th}} \rangle_{\mathrm{s}} \langle \kappa^2 \rangle_{\mathrm{s}}\right]$ seems to be a reasonable approximation in both unity- and non-unity-Lewis-number flames.

2. Flame Front Geometry Evolution

2.1. *Mean Curvature Evolution*

To distinguish curvature evolution in positively and negatively curved flame regions, the generalized iso-surface average of any quantity ϑ (Boger *et al.* 1998) is rewritten as

$$\begin{aligned}
\langle \vartheta \rangle_{\mathrm{s},\Omega} &= \frac{\int_0^1 \int_\Omega F \vartheta \delta(\zeta - \zeta_0) |\nabla \zeta| \, \mathrm{d}V \, \mathrm{d}\zeta_0}{\int_0^1 \int_\Omega F \delta(\zeta - \zeta_0) |\nabla \zeta| \, \mathrm{d}V \, \mathrm{d}\zeta_0} = \frac{\overline{\vartheta |\nabla \zeta|}\Big|_\Omega}{\Sigma_\Omega} \\
&= \frac{\overline{\vartheta |\nabla \zeta|}\Big|_{\kappa^-}}{\Sigma_{\kappa^-}} \cdot \frac{\Sigma_{\kappa^-}}{\Sigma_\Omega} + \frac{\overline{\vartheta |\nabla \zeta|}\Big|_{\kappa^+}}{\Sigma_{\kappa^+}} \cdot \frac{\Sigma_{\kappa^+}}{\Sigma_\Omega} \\
&= \langle \vartheta \rangle_{\mathrm{s},\kappa^-} \cdot \frac{\Sigma_{\kappa^-}}{\Sigma_\Omega} + \langle \vartheta \rangle_{\mathrm{s},\kappa^+} \cdot \frac{\Sigma_{\kappa^+}}{\Sigma_\Omega}.
\end{aligned} \tag{S-2.1}$$

Contributions from both regions to the global flame average may differ due to unequal probabilities of finding negatively/positively curved flame segments, or differences in the conditional averages, or both. In figure S-2 (a) it is shown that in both engine-relevant flame kernel realizations, $\Sigma_{\kappa^-}/\Sigma_\Omega$ is very similar during flame kernel develop-

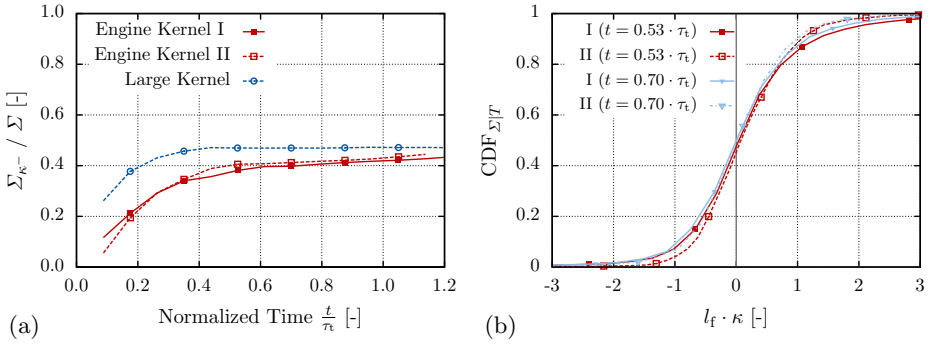

FIGURE S-2. Probability of finding flame surface with negative curvature as function of time (a) and surface-weighted cumulative density functions at two selected time instants (b).

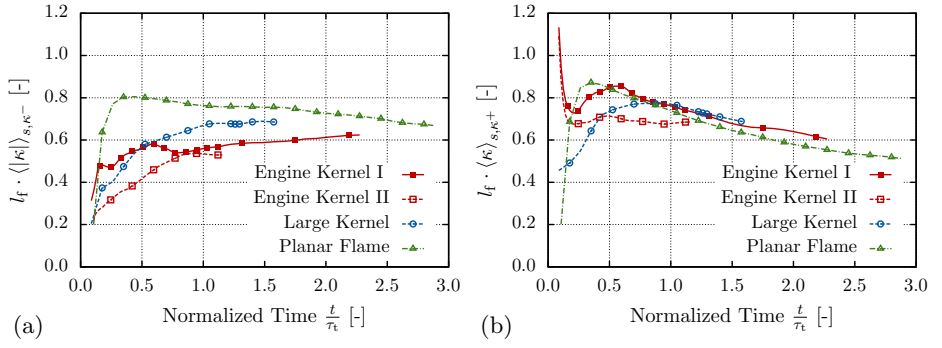

FIGURE S-3. Conditionally surface-averaged curvatures for all flames.

ment. Accordingly, the surface-weighted cumulative density functions (CDFs) of Engine Kernel I and II depicted in figure S-2 (b) are almost identical near $\kappa = 0$. However, the probabilities of finding large negative and positive curvature magnitudes differ between both realizations. At $(t = 0.53 \cdot \tau_t)$, Engine Kernel I has more flame surface with negative and positive curvature radii smaller than the laminar flame thickness. While the fraction of negatively curved kernel surface area of Engine Kernel II has developed to a similar level at $(t = 0.70 \cdot \tau_t)$, Engine Kernel I still features higher probability of finding flame surface with large positive curvature. Consequently, the conditionally averaged flame curvature shown in figure S-3 differs significantly during the early development phase of both engine-relevant flame kernel realizations. Overall, the comparison to the other flame configurations is qualitatively similar to the conditional variance results shown in figure 5 in the paper.

2.2. *Mean Curvature Transport*

To support the discussion of flame curvature transport during flame kernel development (cf. figure 6 in the paper) and to relate the present results to previous studies (Cifuentes *et al.* 2018; Alqallaf *et al.* 2019), the curvature-conditioned mean straining and bending terms due to fluid motion and flame propagation are provided in figure S-4. Note that the data has been evaluated on the temperature iso-surface corresponding to the maximum heat release rate in an unstretched laminar flame. Overall, both engine-relevant flame kernels closely follow the behaviour of the planar flame, with one exception. Shortly after ignition, the bending term due to second derivatives of the fluid velocity (cf. figure S-4 (b))

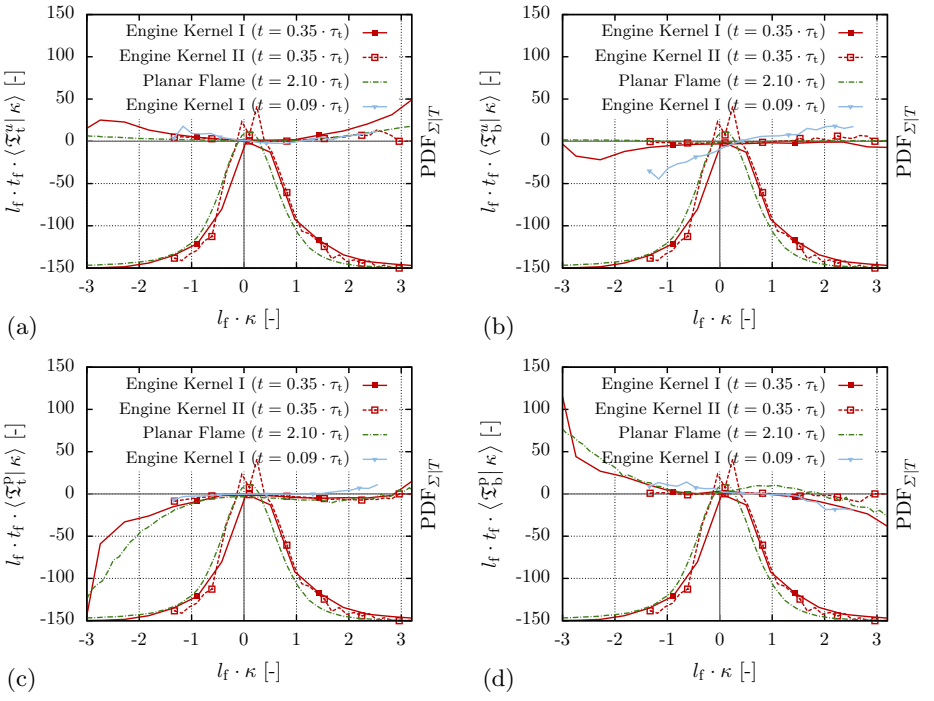

FIGURE S-4. Curvature-conditioned curvature transport terms due to straining (a,c) and bending (b,d) caused by the fluid velocity (a,b) and flame displacement speed (c,d). Data has been conditioned on the temperature iso-surface corresponding to the maximum heat release rate in a laminar unstretched flame.

governs the production of negative curvature in Engine Kernel I. With respect to the production of positive curvature, it is evident from figure S-4 (a) that the on average positive curvature intrinsic to the engine-relevant flame kernel configuration favours the initial amplification of positively curved flame geometry. Further, the reversed flame-propagation straining/bending balance observed when Engine Kernel I exhibits large positive curvature (cf. figure 6 (f) in the paper) can be explained by the change in sign of $\mathfrak{T}_t^p$ at large positive curvatures, as well as the initial deviation of $\mathfrak{T}_b^p$ from the behaviour of a developed flame (cf. figures S-4 (c) and (d)).

2.3. *Skewness of the Mean Curvature Distribution*

2.3.1. *Alignment of Curvature and Strain Principal Axes*

As described in section 4.3 in the paper, large positive curvatures are mainly produced by the tangential strain term in the mean curvature equation. To quantify the length-scale dependence of $\mathfrak{T}_t^u$, one may express mean flame curvature as function of the largest and smallest principal curvature, ($\kappa = k_1 + k_3$). Flame surface regions which feature large positive curvatures will be governed by k_1. Results showing that the corresponding principal direction is mostly aligned with the most compressive principal strain are provided in figure S-5. Since the most compressive principal strain during early flame kernel development is governed by the large-scale flow structures, this phenomenologically demonstrates the major curvature production mechanism. For a quantitative analysis, one may follow the considerations of Pope (1988).

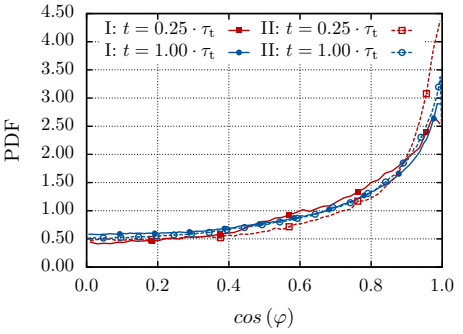

FIGURE S-5. Engine flame kernels: Alignment of the principal axes belonging to the most compressive strain and the most positive curvature at two different times.

2.3.2. *Local Flame-Segment Analysis*

To enable more conclusive analyses, distinctive observations during flame kernel development have been examined in local flame segments extracted from the large reference flames. In this way, fluctuations that are artefacts of the present engine-relevant flame kernel realizations can be distinguished from effects which cannot be observed in developed flames or in flames with larger length scale ratio D_0/l_t. For such analyses, the flow domain of the planar flame was divided into $(N_x \times N_y \times N_z = 1 \times 7 \times 7)$ subsets, where the x-direction is the mean propagation direction of the flame. This number of analysis volumes was chosen, since the instantaneous flame surface area of the planar flame at a characteristic time instant during flame kernel development ($t = 0.6 \cdot \tau_t$) is approximately 49 times larger than the area of the small flame kernel. Expressed in integral length scales, each planar-flame subset contains a mean flame area of $(2\,l_t \times 2\,l_t)$. Similarly, the flow domain of the large flame kernel has been decomposed into $(N_x \times N_y \times N_z = 2 \times 2 \times 2)$ segments.

To investigate if the inversely skewed curvature distribution observed in the early, engine-relevant flame kernel configuration (cf. sect. 4.3 in the paper) is an artefact of the present flame realization or a feature of small flame kernels in general, the flame-segment analysishas been conducted to obtain local curvature distributions from the reference flames. As shown in figure S-6 (a), several segments of the planar flame surface show skewness towards positive curvatures during early turbulent flame development. In some subsets, maximum positive skewness is comparable to the data extracted from the large flame kernel. Hence, the behaviour of the large flame kernel is likely an effect of the particular flame realization. However, the inverse skewness in all planar flame surface segments is much less pronounced than in the small-flame-kernel dataset. Analogously, the flame surface of the large kernel has been divided into sections. In figure S-6 (b), it is apparent that the maximum skewness towards positive curvatures in all analysis volumes of the large flame kernel stays well below the peak reached by the small flame kernel.

By comparison to local regions in both reference flames, it has been confirmed that the occurrence of strong skewness towards positive curvatures is a distinctive feature of the engine-relevant flame kernel configuration.

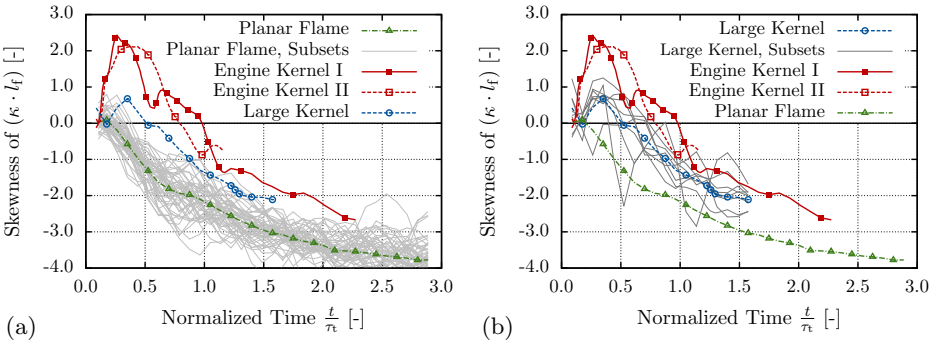

FIGURE S-6. Skewness of surface-averaged curvature for all flames, in comparison to local regions (cf. sect. 2.3.2) in planar flame (a) and local regions in large flame kernel (b).

3. Length-Scale-Dependent Flame Front/Flow Field Alignment

3.1. *Flame Front Alignment with the Unfiltered Flow Field*

In figure S-7, the PDFs of the cosines of the angle between the temperature gradients and the principal axes of the strain tensor are plotted for all flame kernels. The most extensive and most compressive strain eigenvectors are denoted as $s_i^{(1)}$ and $s_i^{(3)}$, respectively. To quantify the temporal development of the scalar fields, alignment statistics have been computed at $(t = 0.25 \cdot \tau_t)$ and $(t = 1.0 \cdot \tau_t)$. At this later time, the three respective PDFs of all flame kernels are in fact quite similar, which indicates that the scalar/flow alignment is already well developed. Preferential alignment with the most compressive strain is observed, which is most pronounced in the large flame kernel dataset. Note that the PDFs have been computed from data points throughout the flame, without conditioning on a particular iso-surface. Results reported by Kim & Pitsch (2007) showed preferential alignment with the most compressive strain at low and high values of the reaction progress variable, as well as at low curvature magnitudes, but less significant. Preferential alignment with the most extensive strain was observed for negative curvatures, as well as for intermediate progress variable values, although much less distinct. Conditional statistics are not considered here for brevity.

At early times, temperature iso-surface orientation is generally much less governed by one principal strain component. In case of the large flame kernel (cf. figure S-7 (c)), angles between the temperature gradient and the most compressive strain eigenvector are mainly very small, since the peak of the corresponding PDF is located very close to unity, similarly to later times. However, the maximum is significantly smaller, since overall, preferential alignment with the most extensive strain is found. This is likely caused by ignition or early heat release and indicates that the ignition kernel determines the orientation of the scalar field. It seems though, that smaller kernel size leads to much less pronounced initial alignment with the most extensive strain (cf. figures S-7 (a) and (b)). Instead, the scalar field orientation of the engine relevant flame kernels mainly follows the most compressive strain. However, significant differences between both small kernel realizations exist at $(t = 0.25 \cdot \tau_t)$. While Engine Kernel II exhibits the most pronounced alignment of all kernels with the compressive principal strain axis, the corresponding alignment PDF of Engine Kernel I peaks at intermediate angles. This characteristic behaviour of Engine Kernel I is in line with its stronger initial deformation (cf. figure 3 in the paper) and can be attributed to preferential alignment with the large flow scales. Regarding alignment with the intermediate principal strain, both flame kernels show similar trends over time.

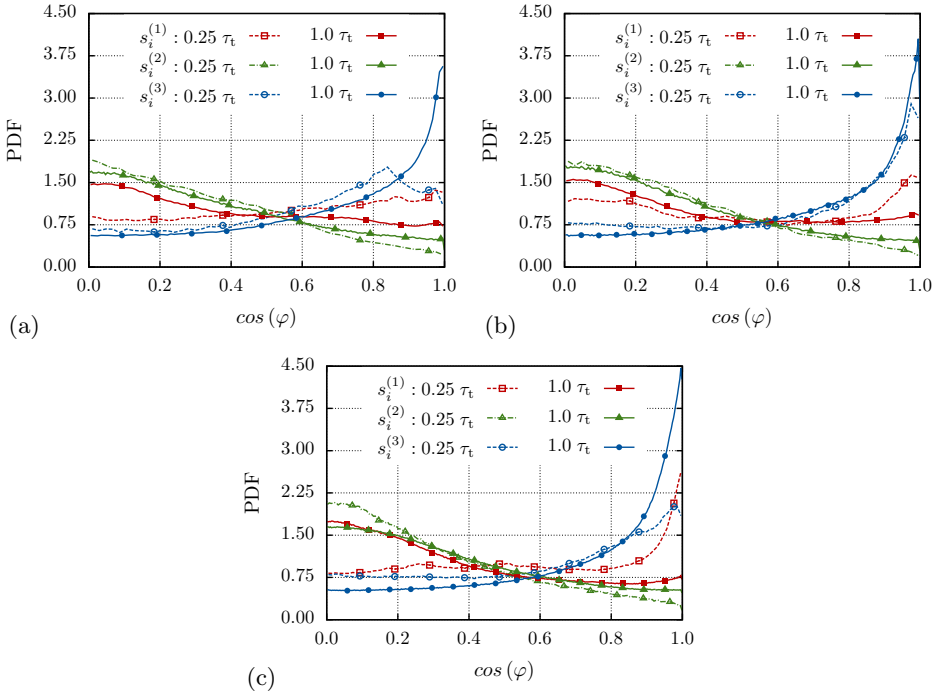

FIGURE S-7. Alignment of scalar gradient and principal axes of strain for Engine Kernel I (a), Engine Kernel II (b) and the large flame kernel (c) at two times. $s_i^{(1)}$: most extensive, $s_i^{(3)}$: most compressive strain.

3.2. *Flame Front Alignment with the Filtered Flow Field*

To illustrate the analysis conducted in §5 of the paper, temperature iso-contours extracted from all three flame kernels at $(t = 0.25 \cdot \tau_t)$ are given in figure S-8. The most compressive principal strain vectors are plotted in the vicinity of the flame contours, scaled by the local strain eigenvalue. In regions of large compressive strain, the flame contour normal vectors are mostly aligned with the depicted principal strain axes. To visualize the effect of large-scale flow structures on the flames, regions that exhibit better alignment of the surface normal vectors with the principal strain axes evaluated from the filtered velocity fields are plotted in black, while regions where better alignment with the unfiltered flow fields is found are plotted in grey colour. Both engine-relevant flame kernels show preferential alignment with large flow scales in significant portions of the flame contours, which is in contrast to the large flame kernel. Since flame kernels have positive mean curvature, the alignment of the flame contours with large-scale flow structures generates flat nibs with very high positive curvature (cf. figures S-8 (a) and (b)).

4. Flame Images

To illustrate early flame kernel development, a sequence of flame images has been extracted from the engine-relevant DNS dataset and is plotted in figure S-9.

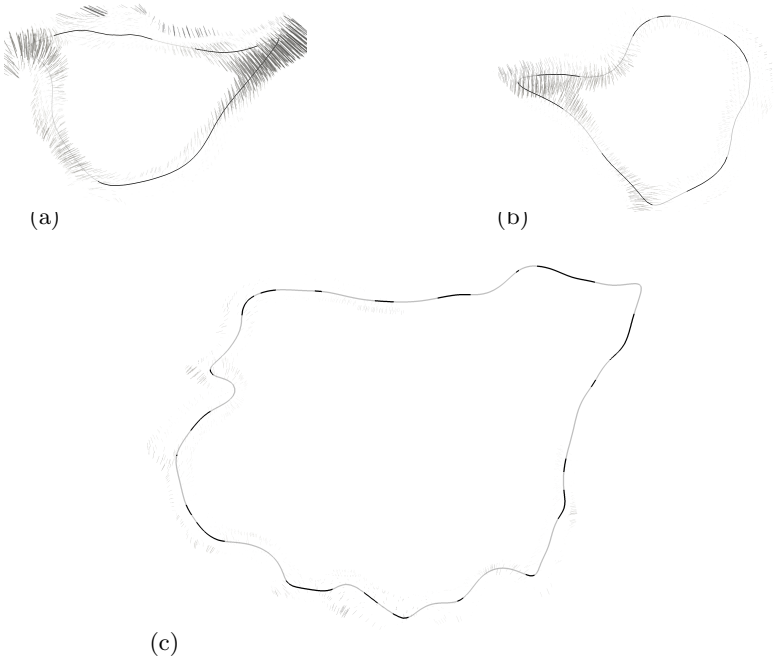

FIGURE S-8. Temperature iso-contours and eigenvectors of the most compressive strain at ($t = 0.25 \cdot \tau_t$). The normal vectors of the black portions of the flame contours are preferentially aligned with the most compressive principal strain computed from a low-pass filtered velocity field. Engine Kernel I (a), Engine Kernel II (b) and the large flame kernel plotted at reduced scale (c).

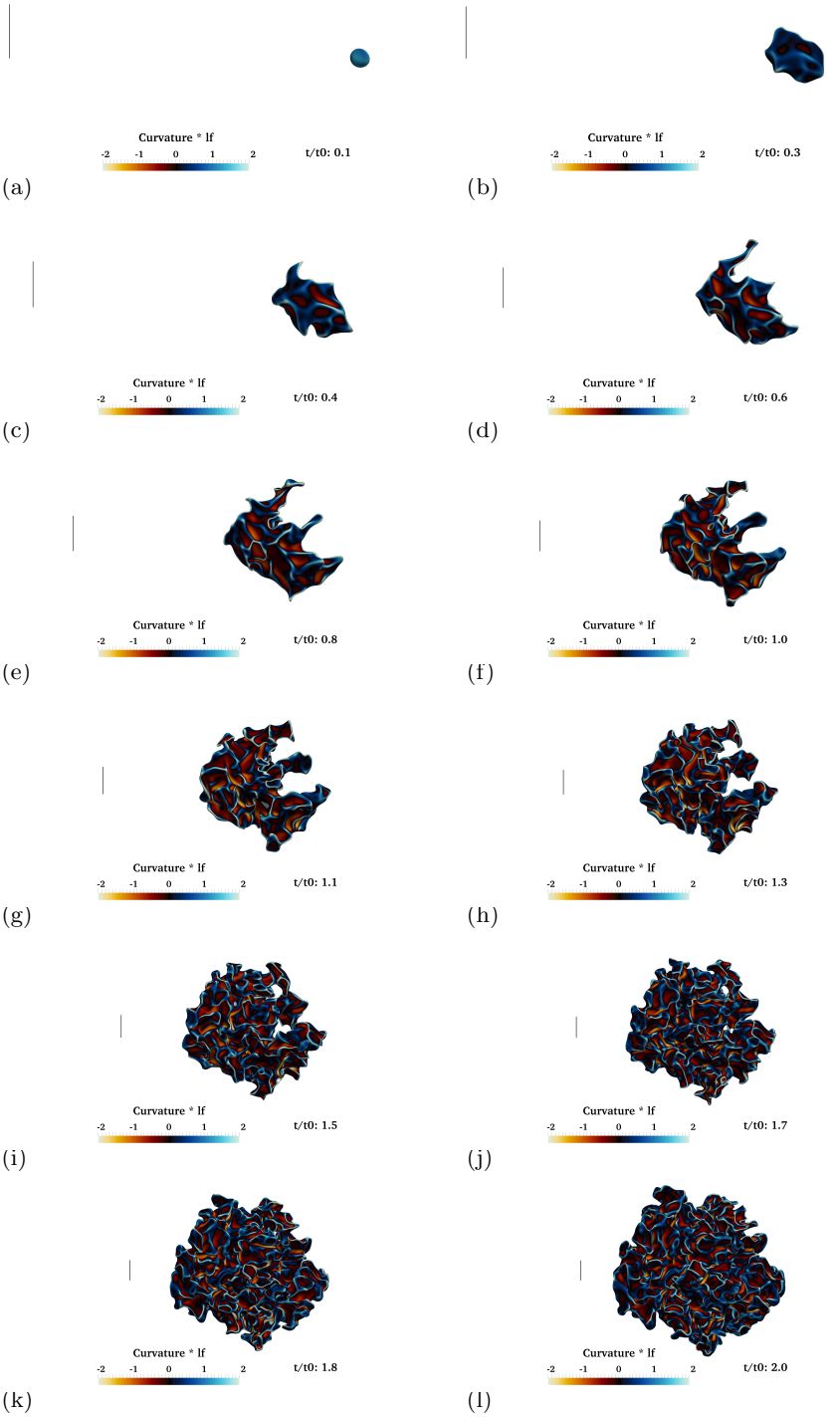

FIGURE S-9. Development of the engine-relevant flame kernel: Temperature iso-contours coloured by flame curvature. The vertical lines illustrate the integral length scale l_t.

REFERENCES

Alqallaf, A., Klein, M. & Chakraborty, N. 2019 Effects of Lewis number on the evolution of curvature in spherically expanding turbulent premixed flames. *Fluids* **4** (1), 12.

Boger, M., Veynante, D., Boughanem, H. & Trouvé, A. 1998 Direct numerical simulation analysis of flame surface density concept for large eddy simulation of turbulent premixed combustion. *Symposium (International) on Combustion* **27** (1), 917–925.

Cifuentes, L., Dopazo, C., Sandeep, A., Chakraborty, N. & Kempf, A. 2018 Analysis of flame curvature evolution in a turbulent premixed bluff body burner. *Physics of Fluids* **30** (9), 095101.

Echekki, T. & Chen, J. 1999 Analysis of the contribution of curvature to premixed flame propagation. *Combustion and Flame* **118**, 308–311.

Falkenstein, T., Kang, S., Cai, L., Bode, M. & Pitsch, H. 2019 DNS study of the global heat release rate during early flame kernel development under engine conditions. *Accepted for publication in Combustion and Flame* , arXiv: http://arxiv.org/abs/1908.07556.

Kim, S. H. & Pitsch, H. 2007 Scalar gradient and small-scale structure in turbulent premixed combustion. *Physics of Fluids* **19** (11), 115104.

Pope, S. B. 1988 The evolution of surfaces in turbulence. *International Journal of Engineering Science* **26**, 445–469.

Wang, H., Hawkes, E. R., Chen, J. H., Zhou, B., Li, Z. & Aldén, M. 2017 Direct numerical simulations of a high Karlovitz number laboratory premixed jet flame – an analysis of flame stretch and flame thickening. *Journal of Fluid Mechanics* **815**, 511–536.